Conditional diffusion machine-learning framework for mapping valence electron distribution from convergent beam electron diffraction

Lijun Wu [1,*] Dmitrii Torbunov [2] Yihui Ren [2] and Yimei Zhu [1,†]

[1] *Condensed Matter Physics and Materials Science Division, Brookhaven National Laboratory, Upton, New York 11973, USA*

[2] *Computing and Data Sciences Directorate, Brookhaven National Laboratory, Upton, New York 11973, USA*

(Received 19 December 2025; accepted 6 April 2026; published 11 May 2026)

Quantitative convergent beam electron diffraction (CBED) enables determination of aspherical valence electron distributions through refinement of low-order structure factors, which are highly sensitive to chemical bonding and charge density variations. However, conventional quantitative CBED (QCBED) requires solving a highly nonlinear inverse problem with many coupled parameters, and computationally intensive dynamical diffraction calculations, making it time-consuming and difficult to apply to complex systems. More broadly, reconstructing charge density and orbital electron distribution from diffraction data has long been a central challenge in both x-ray and electron crystallography. Here, we introduce an artificial-intelligence (AI)-based framework that replaces traditional refinement with a data-driven inverse solver. Using a large synthetic CBED dataset generated by Bloch-wave simulations, we train a conditional diffusion model to directly infer crystal structural parameters and multipole density formalism parameters, and hence valence electron distributions, from CBED patterns alone. By learning from forward simulations across realistic parameter space, the model effectively solves the inverse problem. Compared with direct regression approaches, the diffusion-based framework provides posterior parameter distributions for rigorous uncertainty quantification while preserving quantitative fidelity and reducing analysis time by orders of magnitude. By eliminating the need for external single-crystal x-ray diffraction data and complex nonlinear refinement, this approach enables practical, high-throughput, and *in situ* quantitative CBED, enabling real-time mapping of valence electron distributions and their correlation with functional responses in quantum and energy materials.

DOI: 10.1103/qdpk-6mnv

I. INTRODUCTION

Recent advances in scientific machine learning (ML), artificial intelligence (AI), and exascale computing are creating transformative opportunities for solving inverse problems, inferring system properties from observational data, in increasingly complex domains such as materials, energy, and climate science [1]. Conventional approaches often struggle with strong nonlinearity, limited or noisy data, and the need for rigorous uncertainty quantification. In materials science, these challenges are particularly significant because atomic-scale structure and charge distribution govern key physical properties. Crystal symmetry, lattice distortions, and valence electron redistribution underpin phenomena such as ferroelectric polarization, catalytic activity, superconductivity, and electronic transport. However, reliably measuring these quantities, especially when involving subtle structural distortions or weak redistribution of charge, remains a major experimental challenge.

A central problem in x-ray and electron crystallography is the reconstruction of charge density and orbital electron distributions from diffraction data. Convergent beam electron diffraction (CBED) is uniquely suited to this task because it provides highly localized diffraction information and is sensitive to both structural and electronic features at nanometer and even atomic length scales. Since its development, CBED has been used to determine point-group symmetry, detect polarity, measure strain fields, and quantify charge densities with exceptional precision. Early foundational work by Steeds, Tanaka, Zuo, Spence, and coworkers established CBED and quantitative CBED (QCBED) as indispensable tools for probing low-order structure factors that capture electron bonding, and symmetry-breaking phenomena in crystalline materials [2–4]. Because low-order structure factors encode the valence-electron distribution, their accurate determination through QCBED enables direct insight into bonding configurations, hybridization, and charge transfer in metals, semiconductors, and complex oxides [5–8].

Despite its strengths, conventional QCBED remains difficult to execute. Dynamical electron scattering produces diffraction patterns with rich, highly nonlinear intensity distributions that are extremely sensitive to not only the structure factors but also, for example, crystal thickness, orientation and beam convergence. Extracting quantitative information typically requires extensive Bloch-wave or multislice simulations iteratively fit to experimental patterns. This nonlinear refinement involves many coupled parameters and is often slow, making analysis sluggish and challenging to automate. The computation time and difficulty of the refinement increase exponentially with increasing refinement parameters. Therefore,

*Contact author: ljwu@bnl.gov

†Contact author: zhu@bnl.gov

QCBED is often limited to refine the low-order structure factors that are most sensitive to bonding electrons. To accurately obtain valence electron (VE) distribution, additional multipole density formalism refinement is often required, which usually needs high-order structure factors, e.g., those obtained from x-ray diffraction [3,6,7,9,10]. These limitations have constrained the broader application of QCBED to complex and dynamic materials systems.

Recent advances in AI and ML offer a promising alternative by reframing inverse problems as data-driven inference tasks. By training deep neural networks on large forward-simulated datasets across realistic parameter space, AI models can learn to efficiently invert complex physical processes [11]. In microscopy and diffraction analysis, AI has been demonstrated to replace traditional algorithms for tasks such as crystal symmetry determination, atomic position detection, phase retrieval, orientation mapping, strain mapping, and scattering-pattern classification [12–16]. In the electron microscopy community, these approaches have been successfully applied to scanning transmission electron microscopy (STEM), 4D-STEM, ptychography, and diffraction pattern analysis, significantly accelerating data processing and enhancing robustness against noise and experimental variations [12–20]. These developments offer a compelling opportunity: If AI can disentangle the complexities of dynamical diffraction, it could replace traditional refinement and unlock the full potential of QCBED for high-throughput and real-time charge-density studies.

Building on this progress, we have recently developed machine-learning methods to infer parameters of crystal structure and low-order structure factors from CBED patterns. By extending the conditional diffusion model-based inverse problem solver (CDI) framework from one-dimensional temporal signals to two-dimensional spatial conditioning [21], we demonstrate that the CDI framework not only infers crystal structure and low-order structure factors from CBED patterns, but also provides parameter posterior distributions for uncertainty quantification. In this work, we further extend the CDI framework to predict multipole density formalism (MDF) for directly mapping VE distributions from CBED patterns. By training neural networks on large-scale synthetic CBED datasets generated from Bloch-wave simulations, we demonstrate that AI models can reproduce the accuracy and uncertainty analysis of traditional refinement while providing orders-of-magnitude improvements in speed for many parameters. This enables CBED measurements that were previously impractical, such as directly mapping VE distribution through MDF, *in situ* experiments under AC or GHz-frequency excitations, and combinatorial materials screening. This approach enables rapid mapping of bonding, symmetry, and charge distribution in complex materials and thereby deepens our understanding of the structure–property relationships underlying complex functional materials systems.

II. METHODS

A. Training and testing dataset

The training and testing datasets for machine learning are prepared by CBED simulations which are calculated based on Bloch-wave method [2]. The Bloch-wave calculations fully consider dynamical effect in electron diffraction and have been successfully used for refining low-order structure factors for VE distributions [3,5–7]. Here, we directly use atom-centered multipole density formalism for VE density of crystal. The total electron density of an atom in crystal is [22,23]

$$\rho_{\text{atom}}(r,\theta,\varphi) = P_c\rho_{\text{core}}(r) + P_v\kappa^3\rho_{val}(\kappa r) + \sum_{l=0}^{l_{\max}} \kappa'^3 R_l(\kappa' r) \sum_{m=0}^{l} P_{lm\pm} d_{lm\pm}(\theta,\varphi), \quad (1)$$

where ρ_{core} and ρ_{val} are, respectively, the spherical core and spherical valence electron density, which can be calculated based on multiconfiguration Dirac-Fock wavefunctions [24]. P_c and P_v are the electron population of core and valence component, κ is a parameter describing expansion ($\kappa < 1$) or contraction ($\kappa > 1$) of the valence shell. The third term is the multipole contribution, representing the aspherical distribution of valence electrons. $R_l(\kappa' r)$ is the radial function. θ and ϕ are the angular coordinates of $\boldsymbol{r}$. $d_{lm\pm}(\theta,\varphi)$ and $P_{lm\pm}$ are normalized spherical harmonic density functions and population parameters, respectively. The aspherical x-ray scattering factor is the Fourier transform of the total electron density,

$$f^x(\boldsymbol{g}) = P_c f_c(g) + P_v f_v\left(\frac{g}{\kappa}\right) + 4\pi \sum_{l=0}^{l_{\max}} \sum_{m=0}^{l} P_{lm\pm} i^l \langle j_l(g/\kappa')\rangle d_{lm\pm}(\beta,\gamma), \quad (2)$$

where f_c and f_v are the x-ray scattering factors of spherical core and valence electrons. $\langle j_l(H/\kappa'\rangle$ is the Fourier-Bessel transform of the radial function $R_l(\kappa' r)$. β and γ are the angular coordinates of $\boldsymbol{g}$. The corresponding aspherical electron scattering factor can be calculated based on Mott-Bethe formula,

$$f^e(g) = \frac{m_e e^2}{8\pi\varepsilon_0 h^2}\frac{Z - f^x(\boldsymbol{g})}{s^2}. \quad (3)$$

The structure factors can then be calculated as

$$F_g^e = \sum_j f_j^e(g)\exp(-2\pi i \boldsymbol{g}\cdot\boldsymbol{r_j}) T_j(\mathrm{g}), \quad (4)$$

where r_j and $T_j(g)$ are position and temperature factor of the atom, respectively.

Here as an example, we calculate [010] CBED patterns of magnesium diboride (MgB_2) superconductor for machine learning [25]. MgB_2 has space group P6/mmm with both Mg and B at high symmetry position (Mg at 0,0,0 and B at ⅓,⅔,½ and ⅔,⅓,½). Because of the high symmetry of Mg site (6/mmm) and B site (–6m2), the independent anisotropic Debye-Waller factors (DWF) are u_{11} and u_{33} for both Mg and B ($u_{22} = u_{11}$, $u_{12} = u_{11}/2$, $u_{13} = u_{23} = 0$). The multipole expansion, up to the hexadecapole level, $l_{\max} = 4$, is widely used for VE distribution [26,27]. Because the valence electrons are $3s$ in Mg^{2+}, we set all multipole population to zero for Mg. For B, only quadrupole P_{20}, octupole P_{33+} and hexadecapole P_{40} are allowed for the –6m2 site symmetry. There is only one independent parameter for spherical population: the

TABLE I. Parameter ranges for CBED calculations.

	MDF				DWF Mg (pm^2)		DWF B (pm^2)		Tilt angle (degree)		Thickness (nm)
Parameters	P_v	P_{20}	P_{33+}	P_{40}	u_{11}	u_{33}	u_{11}	u_{33}	θx	θy	t
V	1.5	0.2	0.2	0.2	48	56	47	51	–0.03	0.15	280
ΔV	0.5	0.2	0.2	0.2	25	25	25	25	0.2	0.2	100

spherical population (P_v) of B $2p$ orbital. The spherical population of Mg $3s$ can be calculated based on P_v of B $2p$ with $P_v^{Mg} = 4-2P_v$ to keep the crystal neutral. Therefore, there are eight parameters for structure factors that are off-diagonal elements of the structure matrix in Bloch-wave calculations. The diagonal elements of the structure matrix depend on the beam direction ***K,*** which can be calculated based on tilt angle from the zone axis along horizontal (θx) and vertical (θy) axes. Table I lists these ten parameters and sample thickness with the mean value (V) and range (ΔV) for [010] CBED calculations. The values of the jth ($j = P_v, P_{20}, P_{33+}, P_{40}, u_{11}, \ldots$) parameter in the ith set of parameters for ith CBED pattern calculation is randomly generated as $V_j^i = V_j + R$, where R is a uniform random number in the range of $(-\Delta V_j,\ \Delta V_j)$. One million CBED patterns are calculated for training. Additional 100 000 patterns with the same mean-value and range are calculated for testing.

B. Machine learning

1. Data preprocessing and augmentation

Figure 1(a) shows a typical CBED pattern in the dataset. It consists of 35 slightly overlapping reflection disks with 640 × 640 pixels size. The CBED patterns further undergo preprocessing before model training and evaluation. During training, we apply data augmentation to simulate experimental variability and imperfect data acquisition conditions by randomly rotating ±15° with bilinear interpolation to account for reflection disks misalignment, followed by center cropping to 400 × 400 pixels to match typical experimental field-of-view, and finally randomly cropped to 320 × 320 pixels with scale factors between 0.6–1.0 to simulate variations in microscope magnification and framing. During evaluation, patterns are simply center-cropped to 320 × 320 pixels to simulate typical experimental field-of-view. All models (regression baselines and CDI) use identical preprocessing pipelines for fair comparison.

2. A neural regression baseline

We choose the ResNet-based neural architecture, a *de facto* common choice for image data, as a baseline model for such neural regression tasks [28]. It consists of two parts: a ResNet-based encoder and a multilayer perceptron regression head. The encoder begins with the preprocessed CBED image with 320 × 320 pixel size. An initial convolutional layer extracts 64 learned patterns (also called as features or channels) from the raw pixel data, reducing the spatial resolution to 80 × 80, as shown in Fig. 1(b). The output of this stage is the so-called feature map—a tensor of shape (64, 80, 80) where the first dimension represents the number of extracted patterns, and the last dimensions represent spatial locations for the patterns. The network then processes feature maps through four successive stages. Each stage operates on a principle of hierarchical abstraction—reducing spatial resolution by half while doubling the number of feature channels. This trades spatial detail for representational capacity, allowing the network to capture more abstract information. The key is a "skip connection" that allows information to flow directly through multiple layers, enabling stable training of deep architectures.

The regression head takes the 512-feature map across 10 × 10 spatial dimensions, produced by the ResNet-based encoder, and reduces it to a lower dimension via global average pooling. This produces a 512-dimensional feature vector that summarizes the entire image [Fig. 1(c)]. For the regression baselines, ResNet-50 is used for training because it provides superior overall performance over the other regression baselines. The model is trained for 500 epochs with batch size 32 using the AdamW optimizer with learning rate 10^{-4} and zero weight decay [29]. Training uses 1000 gradient steps per epoch on the training set. Learning rate scheduling uses cosine annealing with $T_{\max} = 500$ epochs. Target parameters are normalized before training using the mean values and ranges listed in Table I. The loss function is mean-squared-error (MSE) computed on normalized parameter predictions. In parameter prediction, a fully connected layer maps the 512-dimensional feature vector to the target physical parameters (thickness, tilt angles, DWFs, and MDFs), as shown in Fig. 1(c).

3. Conditional diffusion model-based inverse problem solver framework

Direct regression only provides single-point prediction without quantitative assessment of parameter uncertainty. This limitation is problematic for quantitative CBED analysis. The CDI framework demonstrates the ability to infer system parameter distributions and their joint correlations from observations of system behavior [21,30]. CDI leverages the inherent stochasticity of the diffusion model process and produces full posterior distributions of system parameters consistent with the data. This enables parameter correlation studies and uncertainty quantification.

At its core, the CDI framework applies diffusion processes directly in the parameter space (**V**) [31]. The framework employs a denoising diffusion probabilistic model (DDPM) [32], conditioned on observational data, to generate parameter distributions consistent with the observations. The DDPM consists of two processes: a forward diffusion process that gradually corrupts parameter vectors with Gaussian noise, and

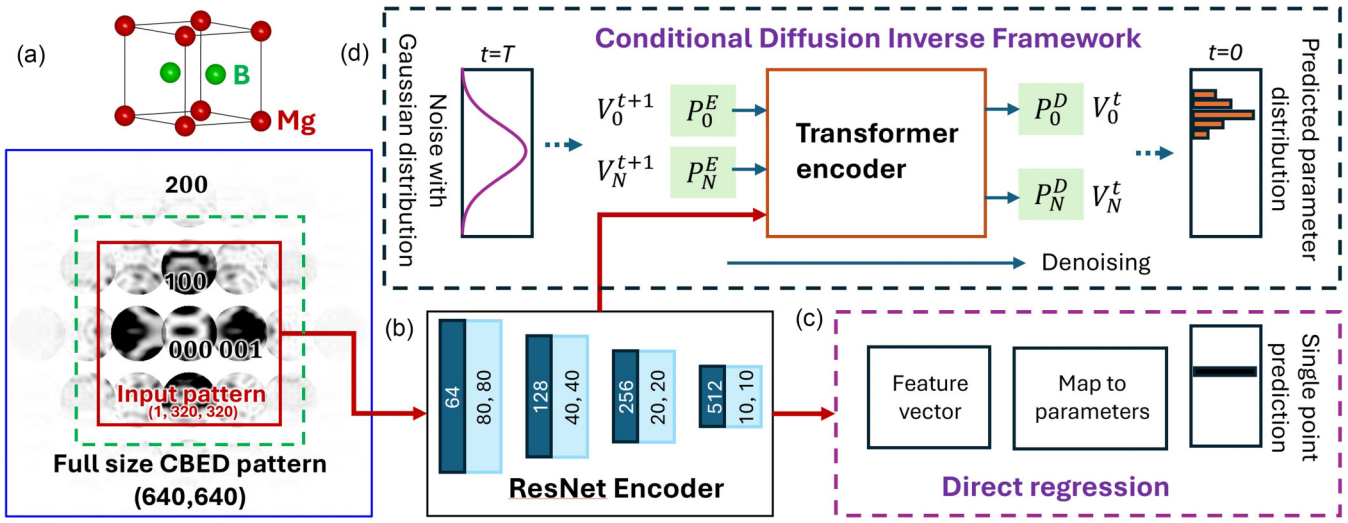

FIG. 1. Conditional diffusion inverse (CDI) and direct regression architectures for CBED parameters (V_0–V_N) inference. (a) A full-size CBED pattern calculated based on MgB_2 crystal with the beam close to [010] direction. The MgB_2 structure model is shown on the top with red and green spheres representing Mg and B atoms, respectively. The input pattern is cropped from a full size (640, 640) CBED pattern. The crop area (red square) with (320, 320) pixel size is randomly picked in the center part with (400, 400) size as marked by green dashed square of the full-size pattern. (b) A ResNet-based encoder processes the CBED pattern and extracts spatial features to the feature maps through (64, 80, 80), (128, 40, 40), (256, 20, 20) to (512, 10, 10). Down-sampling blocks (dark blue) are layers that reduce spatial resolution by half while doubling the number of feature channels. This trades spatial detail for representational capacity, allowing the network to capture more abstract information. Residual blocks (light blue) are complex convolutional neural Network (CNN) blocks that maintain spatial dimensions while refining feature representations. (c) Direct regression: global average pooling averages each of the 512 feature maps across 10×10 spatial dimensions. This produces a 512-dimensional feature vector that summarizes the entire image. Fully connected layer then maps this 512-dimensional representation to the target physical parameters (thickness, tilt angles, DWFs and MDFs). (d) CDI prediction: 1024 random numbers (noise) with a Gaussian distribution (mean $= 0$ and $\sigma = 1$) for each parameter is generated as the parameter tokens for CDI prediction. During reverse diffusion, the transformer encoder iteratively denoises parameter tokens from random noise ($t = T$) to clean estimate ($t = 0$) for posterior distribution of the parameters. Here, t is denoising timestep; V_j^t is the parameter j at time step t; P_j^E and P_j^D are parameter encoder and decoder, respectively.

a learned reverse process that removes this noise to generate parameters consistent with observational data [Fig. 1(d)]. We have extended the CDI framework to 2D image data by replacing the 1D trajectory encoder with a ResNet-based vision encoder while preserving the core transformer-based parameter denoising mechanism [21].

The diffusion model is trained for 1000 epochs with batch size 64 using the AdamW optimizer with learning rate 2×10^{-4} and zero weight decay. Training uses 1000 gradient steps per epoch. No learning rate scheduling is applied. An exponential moving average (EMA) of model weights is maintained with momentum 0.9999. We use a linear noise schedule with T = 800 diffusion timesteps, where $\beta_1 = 2.5 \times 10^{-5}$ and $\beta_T = 0.02$. Target parameters are normalized identically to regression baselines using the mean values and ranges from Table I.

III. RESULTS AND DISCUSSION

A. Performance evaluation

To evaluate the performance between CDI approach and direct regression, we use normalized root mean square error (NRMSE) for parameters comparison,

$$\mathrm{NRMSE}(V_j) = \sqrt{\frac{1}{M}\sum_{i=1}^{M}\left(V_j^i - G_j^i\right)^2} \Big/ {}_{2\Delta V_j}, \qquad (5)$$

where M is number of CBED patterns in the testing dataset. V_j^i and G_j^i are predicted value and ground truth (the value used to calculate the testing CBED pattern) of the jth parameter from ith CBED pattern. ΔV_j is the parameter range listed in Table I. Because the prediction from CDI is a distribution, we use the mean value of that distribution as the V_j^i for CDI. Table II compares performance results across all 11 parameters between regression and CDI baselines. Both regression and CDI methods achieve good NRMSE (<0.12) on MDFs and excellent NRMSE (<0.04) on geometric parameters (thickness and tilt angles) with CDI performance better than that of regression. The NRMSE of the B DWFs is larger than that of Mg DWFs, which can be attributed to the smaller contribution of B in structure factors [Eq. (4)] owing to its smaller scattering factor.

We have evaluated the performance by using full-size CBED pattern for training and prediction, as listed in Table II. The accuracy is improved significantly for MDFs at the expense of computing time. The improvement of the DWFs for Mg u_{11} is also very good, but the others are not so significant as we expected. We also noted that the improvement of DWFs by utilizing full-size CBED with CDI is not as significant as those with regression. This may be due to the weak intensity of the high-order reflection disks when the tilting angles (θ_x, θ_y) are small. We expect that the NRMSE of DWFs can be further reduced with the full-size CBED

TABLE II. NRMSE performance comparison. Lower NRMSE indicates better prediction accuracy.

Model		MDF				DWF Mg		DWF B		Tilt angle		Thickness
		P_v	P_{20}	P_{33+}	P_{40}	u_{11}	u_{33}	u_{11}	u_{33}	θx	θy	t
Crop	Reg.	0.101	0.116	0.109	0.104	0.097	0.171	0.238	0.270	0.029	0.015	0.035
	CDI	0.092	0.107	0.100	0.095	0.087	0.166	0.239	0.268	0.016	0.008	0.013
Full	Reg.	0.081	0.078	0.080	0.076	0.055	0.137	0.194	0.209	0.016	0.010	0.011
	CDI	0.073	0.068	0.069	0.066	0.069	0.161	0.211	0.232	0.013	0.007	0.006

patterns by increasing the tilting angle range in the training and testing dataset to increase the intensity of high-order reflection disks.

B. Uncertainty quantification evaluation

The CDI framework generates parameter distributions conditioned on observational data, which can be used for evaluating uncertainty of the prediction. In CDI prediction, we use 1024 random numbers (noise) with Gaussian distribution (mean $= 0$ and $\sigma = 1$) for each parameter as the initial parameter tokens for CDI prediction. After reverse diffusion on a testing CBED pattern, we obtain posterior distribution with 1024 samples for each parameter. Figure 2 shows the histograms of posterior distributions from the prediction of a single CBED pattern. In general, each histogram shows a Gaussian-like peak with its mean (down arrow) close to the ground-truth value (upper arrow), indicating a confident prediction for these parameters. The wider DWF peaks of B can be attributed to the smaller contribution of B to CBED intensity, consistent with NRMSE analysis. The peak of the sample tilt and thickness is very sharp, indicating excellent predictions for sample geometries.

The posterior distributions vary with testing CBED patterns; we use two well-established metrics: calibration and sharpness to quantify the uncertainty from the testing dataset [21,33,34]. The empirical coverage probability measures the actual frequency at which the true parameter falls within a confidence interval, defined by confidence level α. Figures 3(a)–3(c) show calibration plots calculated based on CDI posterior distributions of parameters over 1024 CBED testing patterns. The results indicate well-calibrated uncertainty estimates for MDFs [Fig. 3(a)] and DWFs [Fig. 3(b)], as they are almost on the diagonal lines which indicate perfect calibration. Geometric parameters [sample thickness and tilt angles, Fig. 3(c)] exhibit slight miscalibration, with expected coverage error around 6–12%. This may reflect challenges in modeling very sharp posterior

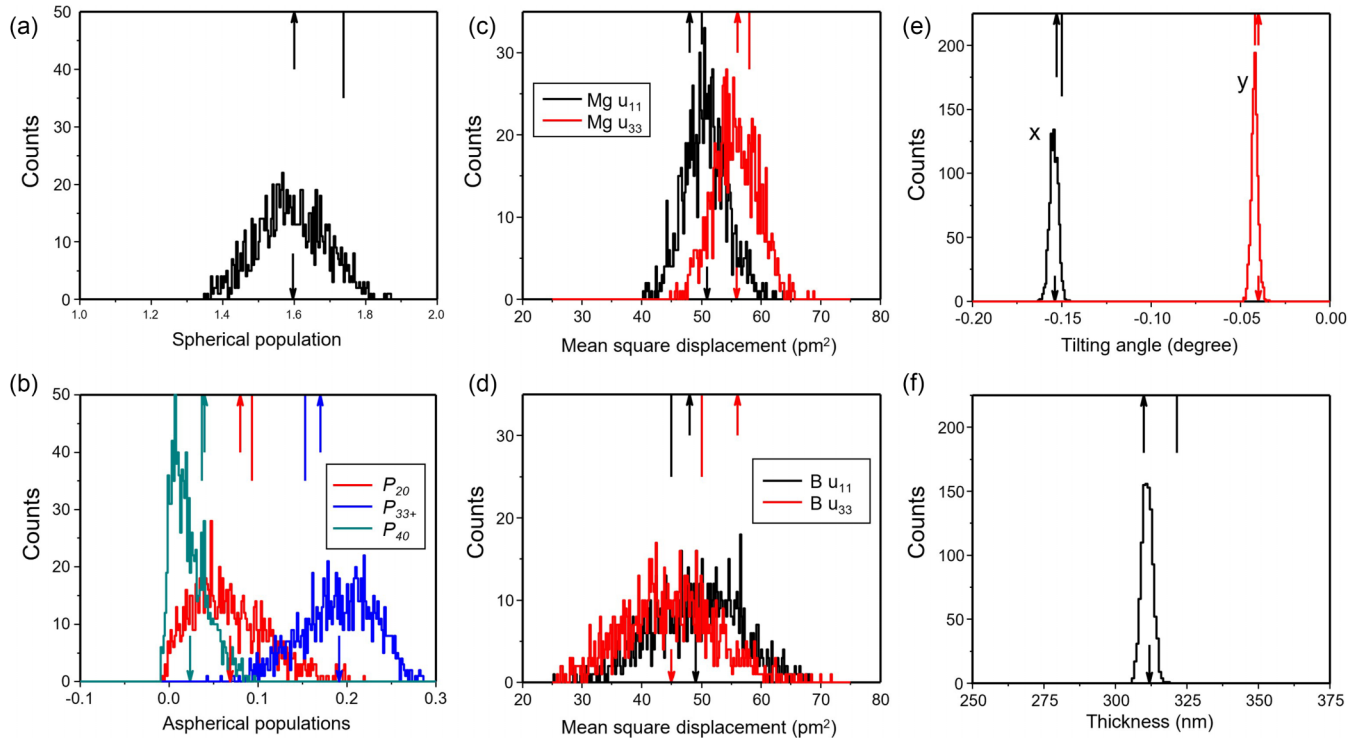

FIG. 2. Posterior distributions from a single CBED pattern by CDI prediction. (a) Spherical population of B 2p orbital and (b) aspherical population of B 2p quadrupole (P_{20}, red), octupole (P_{33+}, blue), and hexadecapole (P_{40}, green). (c), (d) DWFs of (c) Mg and (d) B. (e) Tilting angles and (f) thickness. The same-colored up arrows and down arrows point to the corresponding ground-truth values (the parameters used to calculate the testing CBED pattern) and mean values, respectively. Vertical lines indicate the point values predicted by direct regression (see Table III for their values).

TABLE III. Mean and standard deviation (STD) from distributions shown in Figs. 2 and 4. Ground truth and predicted values from single-pattern regression are also listed.

		MDF				DWF_{Mg} (pm^2)		DWF_B (pm^2)	
Model		P_v	P_{20}	P_{33+}	P_{40}	u_{11}	u_{33}	u_{11}	u_{33}
Ground truth		1.6	0.08	0.17	0.04	48	56	47	51
Single regression		1.738	0.093	0.153	0.037	49.9	58.2	45.2	49.8
Single CDI	Mean	1.596	0.069	0.191	0.024	50.9	55.9	48.9	44.9
	STD	0.096	0.042	0.041	0.020	3.6	3.7	7.7	7.8
Regression	Mean	1.625	0.084	0.170	0.053	50.6	56.8	49.4	50.5
	STD	0.060	0.037	0.031	0.032	3.8	4.1	5.9	6.3
CDI	Mean	1.618	0.090	0.172	0.044	51.2	57.2	43.3	53.4
	STD	0.054	0.025	0.019	0.022	3.4	3.8	6.7	6.5

distributions for well-constrained parameters, potentially because of high sensitivity of diffraction intensity to crystal orientation and thickness whose predictions remain highly accurate (Table II).

Sharpness quantifies the precision of uncertainty estimates by measuring the width of the prediction interval. Sharp predictions provide narrow confidence intervals while maintaining proper coverage. We calculate normalized sharpness as the average interval width over the testing dataset [21],

$$\text{Sharpness}(V_j) = \frac{1}{2M\Delta V_j}\sum_{i=1}^{M} CI_\alpha\left(V_j^i\right), \tag{6}$$

where $CI_\alpha(V_j^i)$ is the width of the confidence interval for predicted value V_j^i. M is number of CBED patterns in the testing dataset. ΔV_j is the parameter range listed in Table I.

Figures 3(d)–3(f) show coverage probability versus normalized sharpness for predicated parameters calculated based on CDI posterior distributions of parameters over the same 1024 CBED testing patterns. The normalized sharpness is satisfactory for the MDF parameters and the Mg DWFs over the explored parameter range, indicating confident predictions. This assessment is consistent with the narrow peak widths of their posterior distributions shown in Fig. 2. In contrast, the sharpness for the B DWFs is poor, which can be attributed to the smaller contribution of B atoms to the CBED intensity, consistent with the corresponding NRMSE values. The sharpness of the sample geometric parameters is exceptionally high, particularly for the sample orientation, consistent with the high sensitivity of CBED intensity to sample geometry and demonstrating excellent predictive accuracy for these parameters.

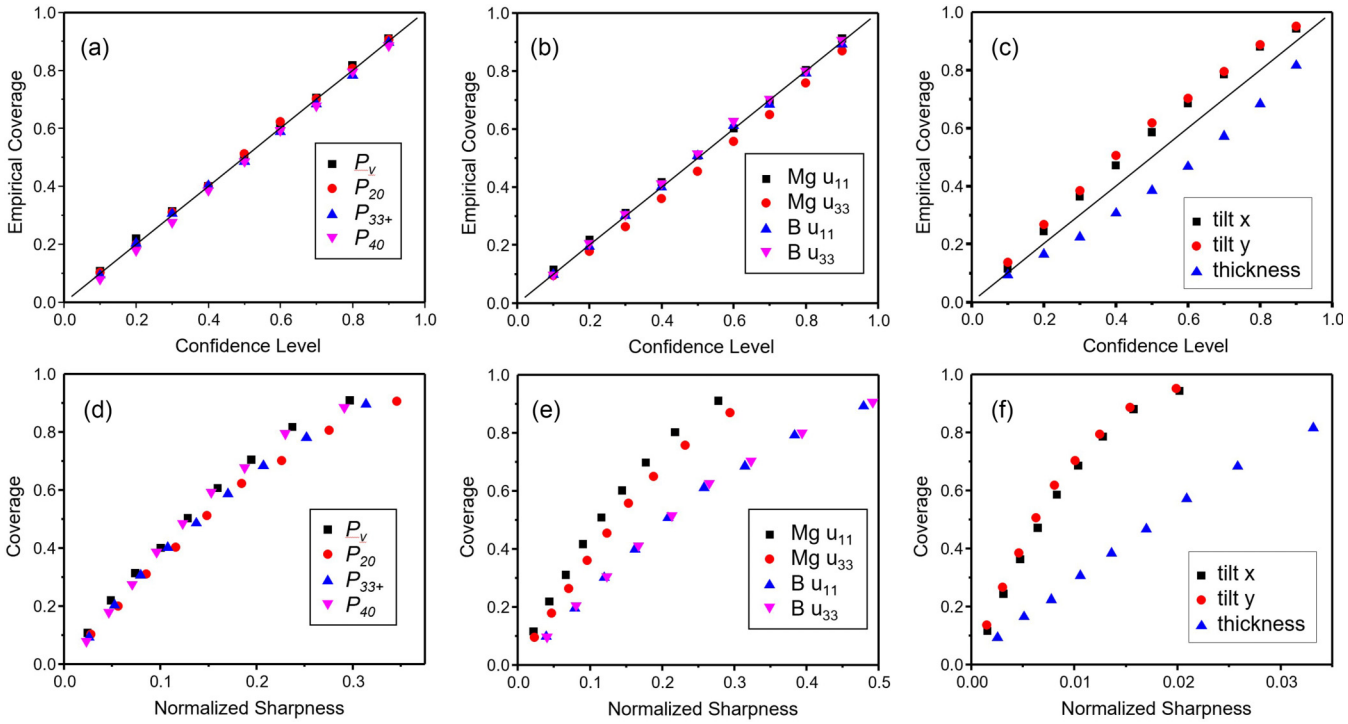

FIG. 3. (a)–(c) Empirical coverage probability as a function of predicted confidence levels for parameters of (a) MDFs, (b) DWFs and (c) sample geometry. Diagonal lines indicate perfect calibration. (d)–(f) Coverage as a function of normalized sharpness for parameters of (d) MDFs, (e) DWFs, and (f) sample geometry.

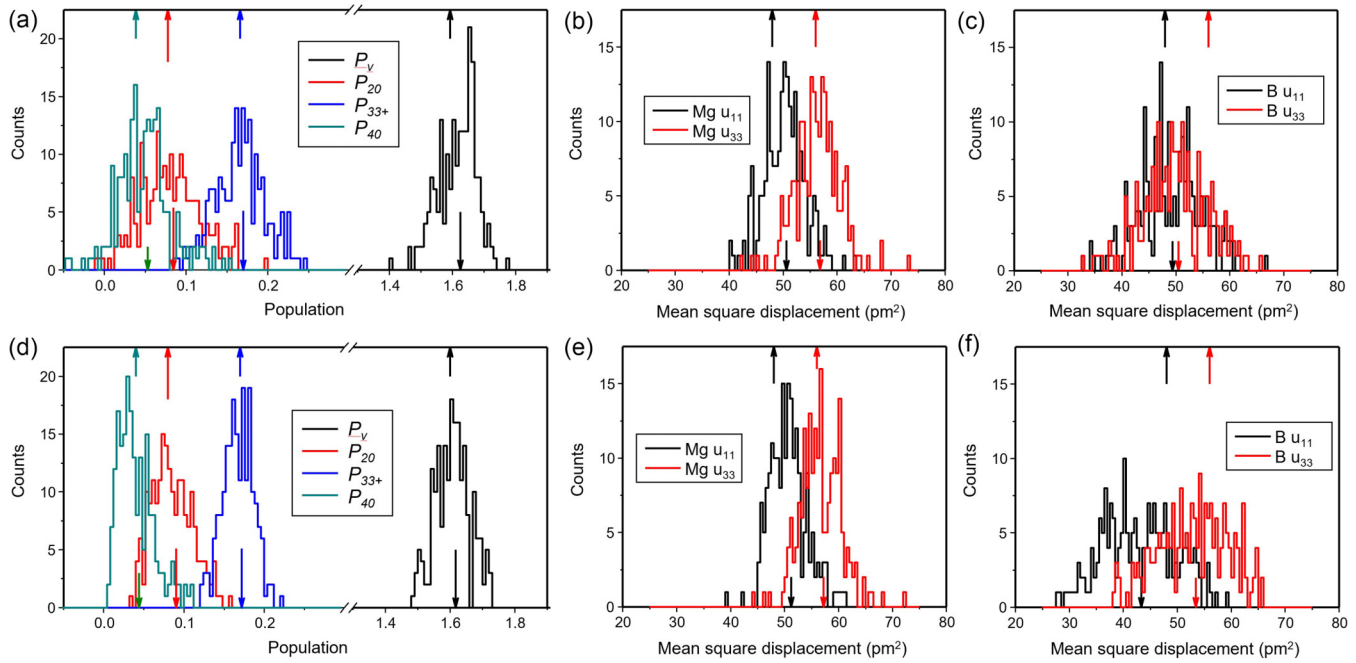

FIG. 4. Parameter distributions from a testing dataset with 200 CBED patterns by (a)–(c) direct regression and (d)–(f) CDI predictions. (a), (d) Spherical population of B 2*p* (black) and aspherical population of B 2*p* quadrupole (P_{20}, red), octupole (P_{33+}, blue), and hexadecapole (P_{40}, green). (b), (c), (e), (f) DWFs of (b), (e) Mg and (c), (f) B. The same-colored up arrows and down arrows point to the corresponding ground truth and mean values (see Table III for their values), respectively.

The uncertainty can be also evaluated by statistical standard deviation (STD), which is widely used in traditional CBED refinements where many experimental CBED patterns are refined for the low-order structure factors [6,25]. The standard deviation from the posterior distribution shown in Fig. 2 is listed in Table III. This is from a single CBED pattern. For similar standard deviation analysis for parameters from multiple CBED patterns, we generate another testing dataset containing 200 CBED patterns calculated with fixed value of MDF and DWF as listed at the ground-truth row in Table III. The tilting angles and thickness are randomly sampled with the same range in Table I, reflecting the variation of the crystal orientation and thickness in experiments. Figure 4 shows the distributions of the predicted parameters over this testing dataset. We use mean value of the posterior distribution for each CDI prediction for Figs. 4(d)–4(f). Compared to the posterior distribution from a single CBED prediction, the peak from the predictions of multiple CBED patterns is sharper and its mean value is closer to the ground-truth value. This can be clearly seen in their standard deviations listed in Table III.

C. Performance from simulated CBED testing patterns

Figures 5(a) and 5(b) show the predicted CBED patterns calculated based on parameters from single-point value predicted by single-pattern regression [Fig. 5(a)] and mean value from posterior distribution predicted by single-pattern CDI [Fig. 5(b)], as listed in Table III and marked by solid lines and down arrows in Fig. 2. The original pattern used for prediction is a simulated pattern and shown in Fig. 5(c) for comparison (its parameters are listed at the row of ground truth in Table III). While the predicted pattern by single-pattern regression [Fig. 5(a)] only shares the main features as those in the original pattern [Fig. 5(c)], the pattern predicted by single-pattern CDI agrees with the original pattern excellently, indicating that the CDI method can infer the parameters quantitatively.

With MDFs, the structure factors and VE density of the crystal can be calculated together based on Eq. (1)–(4). The values of the spherical and aspherical populations of B are estimated from our measured structure factors and are listed in the ground-truth row in Table III. The structure factors calculated by these values of populations are –0.21, 0.94, 2.61 and 2.93 for 001, 100, 101, and 002 reflections, respectively, which basically equal to the structure factors we measured [25]. Figure 6(a) shows the static VE distribution at (110) plane through Mg and B atoms calculated based on MDF, revealing the aspherical orbital feature of B 2*p*. In contrast, the VE distribution calculated based on independent atomic model [IAM, inset of Fig. 6(a)] exhibits spherical distribution for both Mg and B. Figure 6(b) shows the static deformation density map, which is the map by subtracting the IAM map from the MDF map. The deformation map reveals the major VE distribution feature, consistent with that calculated by density functional theory (DFT), e.g., high electron density between B-B, but lacks the fine feature especially close to the atomic core because of the limited multipole terms, e.g., only up to hexadecapole ($l_{\max} = 4$) is used here. We have calculated deformation maps based on predicted MDF parameters listed in Table III. Figures 6(c)–6(f) show the difference between predicted map and the ground-truth map in Fig. 6(b). All predicated deformation maps [insets in Figs. 6(c)–6(f)] visually agree with the ground-truth map [Fig. 6(b)] very well. Only the single-pattern regression shows relatively large residual contrast in the difference map with maximum

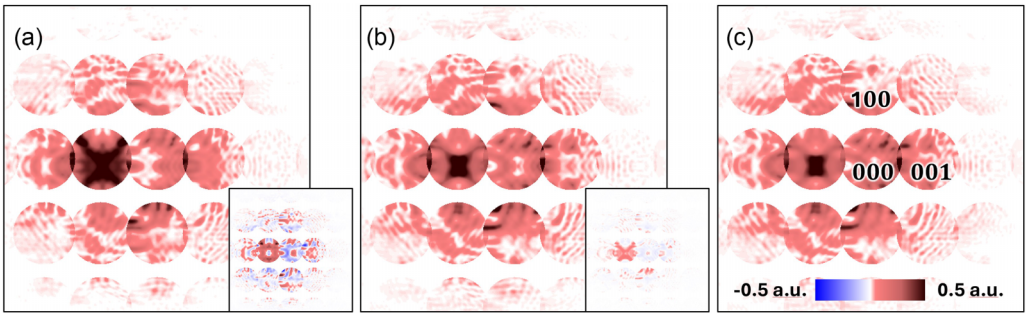

FIG. 5. CBED patterns calculated with parameters predicated by regression (a) and CDI (b). (c) Original CBED pattern used for predictions. The crystal is tilted 0.15° from [010] zone, resulting in asymmetric intensity distribution in the CBED patterns. The insets in (a) and (b) are the difference between (a) and (c), and (b) and (c), respectively. The CBED pattern calculated by CDI parameters agrees with the original pattern very well.

difference $0.028\,\mathrm{e}/\mathrm{Å}^3$ at positions indicated by arrows in Fig. 6(c), corresponding to about a 15% deviation from the ground-truth map [Fig. 6(b)]. This indicates relatively poor accuracy in MDF prediction when single-pattern regression is used. The maximum difference [Fig. 6(d)] for single-pattern CDI is $0.013\,\mathrm{e}/\mathrm{Å}^3$, corresponding to about 7% deviation. When multiple CBED patterns are used, the maximum deviation is reduced to below 5% [Figs. 6(e)–6(f)]. This points out the importance of using multiple CBED patterns for inferencing MDF parameters for accurate and reliable VE density mapping. In practice, this is not a limitation because the samples studied typically exhibit bending and thickness variations. As a result, acquiring multiple CBED patterns with varying crystal orientations and thicknesses is straightforward by simply moving the sample, and generating predictions for multiple CBED patterns is fast and efficient. In contrast, performing traditional refinement for a large number of CBED patterns is computationally intensive and time-consuming.

D. Performance from experimental CBED pattern

Figure 7(a) shows an experimental [010] zone CBED pattern of MgB_2 acquired using the JEOL-3000F with a beam energy of 297 keV. The *00l* reflections row is rotated from the horizontal axis by 4.8°. The disk shape is elliptical, indicating that the pattern is slightly distorted due to the aberrations of the electron optics of the instrument. Although our CDI framework is trained with image rotation (±15°) and dimension variation (scale factor 0.6–1.0), the prediction directly from this CBED pattern is not good, as the posterior distributions of the inferred parameters are rather poor without distortion correction. Figure 7(b) shows the distortion

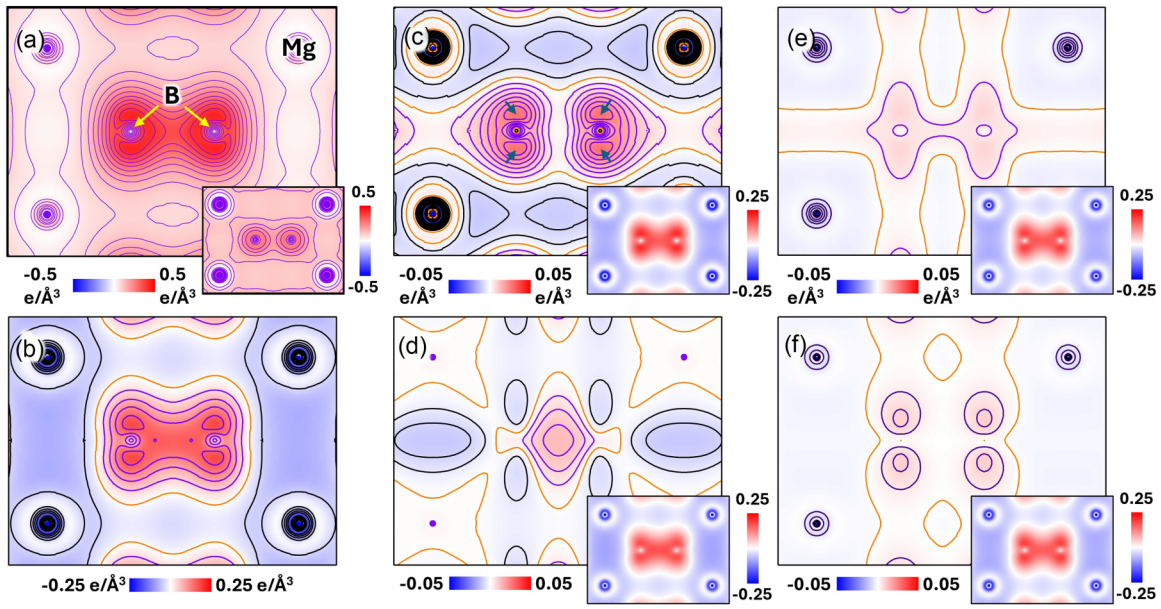

FIG. 6. (a) Static valence and (b) deformation electron-density maps at (110) plane through Mg and B atoms calculated based on MDF with the parameters of ground truth listed in Table III. The arrows in (a) point to the B sites. The inset in (a) is the valence electron-density map calculated based on IAM model. (c)–(f) Difference maps between (b) and those calculated by predicted parameters of (c), (e) direct regression and (d), (f) CDI from (c), (d) single CBED pattern and (e), (f) 200 CBED patterns. The insets are corresponding static deformation maps. Maps are overlapped with contours with intervals of (a), (b) $0.04\,\mathrm{e}/\mathrm{Å}^3$ and (c)–(f) $0.004\,\mathrm{e}/\mathrm{Å}^3$, respectively. The black, orange, and purple contours correspond to density difference $\Delta\rho < 0$, $\Delta\rho = 0$, and $\Delta\rho > 0$, respectively.

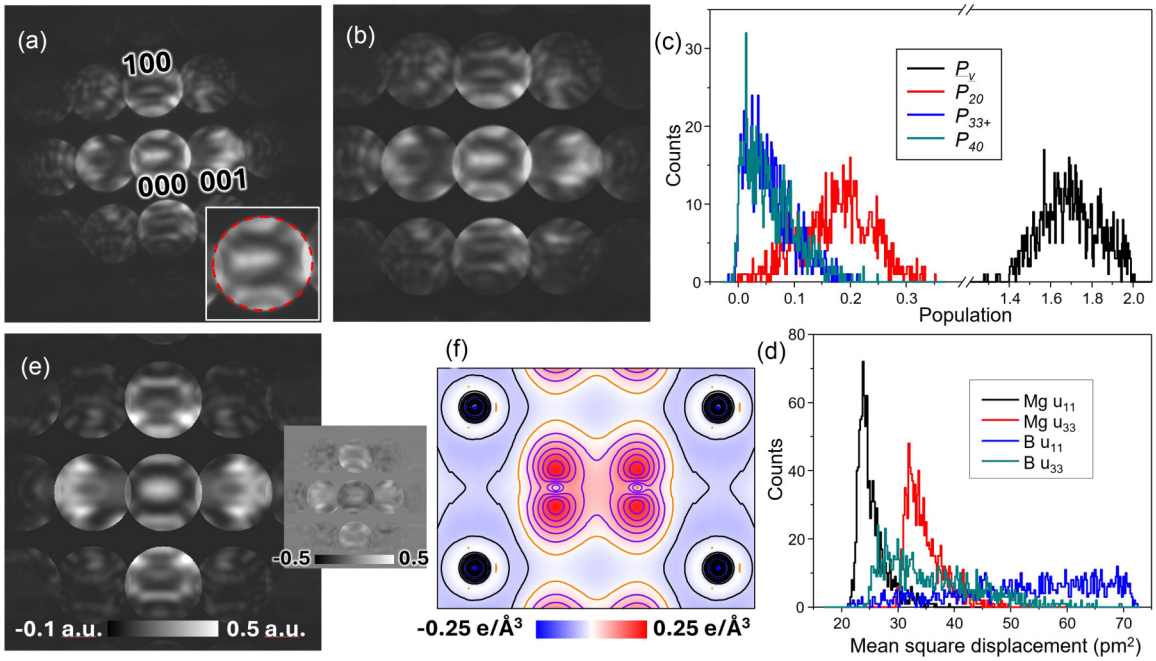

FIG. 7. (a) An experimental CBED pattern acquired from MgB_2 superconductor at room temperature along [010] zone axis. The pattern is slightly distorted as the disk is elliptical. The inset shows the magnified 000 disk overlapped with a dashed ellipse with aspect ratio of 1.065. (b) The distortion corrected pattern after a bilinear warp function transformation from (a). (c), (d) Posterior distributions of (c) B $2p$ valence population (black, spherical; red, quadrupole P_{20}; blue, octupole P_{33+}; and green, hexadecapole P_{40}) and (d) thermal vibration (black, Mg u_{11}; red, Mg u_{33}; blue, B u_{11}; and green, B u_{33}) from the distortion-corrected CBED pattern in (b) by CDI prediction. (e) CBED pattern and (f) static deformation electron-density map at (110) plane calculated based on the inferred parameters listed in Table IV. The inset in (e) is the difference between (e) and (b). The deformation map is overlapped with contours with intervals of 0.04 e/Å^3. The black, orange, and purple contours correspond to density difference $\Delta\rho < 0$, $\Delta\rho = 0$, and $\Delta\rho > 0$, respectively.

corrected pattern obtained using a bilinear warp function, which adjusts the elliptical disks to have a unity aspect ratio. By using this distortion corrected CBED pattern in the trained CDI framework, we obtained the posterior distribution for B $2p$ populations and DWFs of Mg and B, as shown in Figs. 7(c) and 7(d). The mean values and standard deviations are listed in Table IV. The posterior distributions are well defined for B $2p$ valence electron populations and DWFs of Mg but are poor for DWFs of B [blue and green lines in Fig. 7(d)]. This can be attributed to the small contribution of B to structure factors, especially at low order. The sensitivity of the DWFs to the structure factors increases with scattering angle. Therefore, high-order reflections must be included in CBED patterns when high-precision DWFs are required.

The structure factors calculated with the inferred parameters are –0.30, 0.91, 2.65, and 2.99 for 001, 100, 101, and 002 reflections, respectively, which are close to the values in our previous refinement [25]. Figure 7(e) is the simulated CBED pattern calculated based on the inferred mean values, which agrees with the experimental pattern [Fig. 7(b)] very well. This confirms capability of the CDI framework in quantitative analysis of CBED patterns. Figure 7(f) is the static deformation density map calculated from the inferred MDF parameters. It shows B-B bonding, being consistent with that calculated by DFT.

So far, our machine-learning algorithm has been developed and trained on simulated datasets, and deployed on test datasets also generated from simulations. When applied to experimental CBED patterns, any systematic difference between the simulations (training dataset) and the experimental patterns (test dataset) may severely degrade the algorithm performance on the parameter inference. This issue is known as the domain shift problem [35,36]. The differences between simulated and experimental CBED patterns may include image distortion, noise, phonon diffuse scattering induced background, data dynamic range, and other factors. In the example above, we map experimental data into the simulated data domain using a bilinear warp function to correct image

TABLE IV. Mean and standard deviation from the posterior distributions inferred by CDI from a distortion corrected experimental pattern in Fig. 7(b).

	MDF				DWF_{Mg} (pm^2)		DWF_B (pm^2)	
	P_v	P_{20}	P_{33+}	P_{40}	u_{11}	u_{33}	u_{11}	u_{33}
Mean	1.70	0.18	0.06	0.06	25.5	35.1	52.9	36.3
STD	0.14	0.06	0.04	0.04	2.5	3.5	12.8	8.5

distortion and a scale factor to adjust the data dynamic range. This approach yields reasonably good parameters inference although it requires adjustment of the bilinear parameters and the scale factor prior to inference. The inference could be further improved by accounting for radial and spiral lens distortions [4]. Energy filtered CBED patterns can also help to reduce phonon diffuse scattering.

Conversely, translating simulated data into a real-world domain can increase the realism of the simulated dataset and reduce systematic uncertainties. We have trained the model with image rotation, shift, and magnification; however, this is not sufficient for accurate parameters inference on experimental CBED patterns. Incorporating lens distortion, noise, and data dynamic range scaling into the training dataset would greatly improve both precision and efficiency of prediction from experimental CBED patterns. Because the shape and position of the reflection disks are well defined in the CBED patterns, we can actually train the neural network by acquiring many experimental CBED patterns to correct the instrument-induced distortion and noise [37–39]. This would outperform the simple correction by using bilinear warp function or radial and spiral lens distortions.

The training time for the CDI network depends on the computer power and size of the dataset. It takes about 93 h to train a model based on a training dataset with one million CBED patterns on a single NVIDIA RTX A6000 GPU. Once the model is properly trained, the inference is quick and can be performed in the less powerful computer. A single inference on a given CBED pattern takes about 2.35 s. The inference time can be further improved by using batched inference for posterior distribution of CDI, e.g., it takes about 55 s to obtain the posterior distributions with 1024 samples from a CBED pattern on a single NVIDIA RTX 3090 GPU. This outperforms traditional refinement where the refinement for each CBED pattern requires determining initial parameters and many iterations for convergence. The high efficiency of the ML inference would make QCBED analysis more accessible and could widely expand its applications, e.g., in complex crystal with large unit cells in which the traditional refinement is very difficult or slow owing to increased parameters.

IV. CONCLUSIONS

In this work, we have demonstrated that machine-learning approaches provide a powerful alternative to conventional QCBED refinement for extracting structural and electronic parameters from CBED data. By training on extensive synthetic datasets generated via Bloch-wave simulations, we show that both regression-based neural networks and conditional diffusion inference frameworks can reliably extract parameters relevant to QCBED analysis, with the CDI framework offering superior performance. In particular, the diffusion-based approach yields posterior parameter distributions, enabling rigorous uncertainty quantification, an essential capability when experimental CBED patterns are limited in number, affected by noise and distortion, or acquired under constrained conditions.

Beyond accelerating conventional workflows, the AI-assisted framework fundamentally extends the scope of QCBED. Rather than refining only a small subset of low-order structure factors, the proposed approach directly infers MDF parameters from CBED patterns alone, enabling quantitative reconstruction of valence electron distributions without reliance on complementary single-crystal x-ray diffraction measurements. This capability significantly broadens the applicability of valence-electron mapping to complex materials systems that are inaccessible to traditional methods.

Owing to its inference speed, robustness, and tolerance of structural complexity and experimental imperfections, the AI-driven QCBED framework is well suited for high-throughput and *in situ* investigations, as well as for probing charge transfer across interfaces, defects, heterostructures, and other nanoscale environments. More broadly, data-driven inverse solvers enable real-time, spatially resolved mapping of bonding and electronic structure across a wide range of quantum, electronic, and energy materials.

ACKNOWLEDGEMENT

This work was supported by the US Department of Energy, Office of Science, Basic Energy Science, Division of Materials Science and Engineering, under Contract No. DE-SC0012704.

DATA AVAILABILITY

The data that supports the findings of this article cannot be made publicly available because of their large volume. The data are available upon reasonable request from the authors.

[1] J. Donatelli *et al.*, Basic research needs for inverse methods for complex systems under uncertainty, Technical Report, US Department of Energy (USDOE), Washington, DC, Office of Science, Advanced Scientific Computing Research (ASCR) (2025), https://doi.org/10.2172/2583339.

[2] J. C. H. Spence and J. M. Zuo, *Electron Microdiffraction*, (Plenum Press, New York, 1992).

[3] J. M. Zuo, M. Kim, M. O'Keeffe, and J. C. H. Spence, Direct observation of *d*-orbital holes and Cu-Cu bonding in Cu_2O, Nature (London) **401**, 49 (1999).

[4] K. Tsuda and M. Tanaka, Refinement of crystal structural parameters using two-dimensional energy-filtered CBED patterns, Acta Crystallogr. Sect. A **55**, 939 (1999).

[5] K. Tsuda, Y. Ogata, K. Takagi, T. Hashimoto, and M. Tanaka, *et al.*, Refinement of crystal structural parameters and charge density using convergent-beam electron diffraction - the rhombohedral phase of $LaCrO_3$, Acta Crystallogr. Sect. A **58**, 514 (2002).

[6] J. C. Zheng, A. I. Frenkel, L. Wu, J. Hanson, W. Ku, E. S. Božin, S. J. L. Billinge, and Y. Zhu, Nanoscale disorder and local electronic properties of $CaCu_3Ti_4O_{12}$: An integrated study of electron, neutron, and x-ray diffraction, x-ray absorption fine structure, and first-principles calculations, Phys. Rev. B **81**, 144203 (2010).

[7] C. Ma, L. Wu, W.-G. Yin, H. Yang, H. Shi, Z. Wang, J. Li, C. C. Homes, and Y. Zhu, Strong coupling of the iron-quadrupole and

anion-dipole polarizations in $Ba(Fe_{1-x}Co_x)_2As_2$, Phys. Rev. Lett. **112**, 077001 (2014).

[8] L. J. Wu, Y. M. Zhu, and J. Tafto, Test of first-principle calculations of charge transfer and electron-hole distribution in oxide superconductors by precise measurements of structure factors, Phys. Rev. B **59**, 6035 (1999).

[9] T. T. Shang, D. Xiao, F. Meng, X. Rong, A. Gao, T. Lin, Z. Tang, X. Liu, X. Li, Q. Zhang, *et al.*, Real-space measurement of orbital electron populations for $Li_{1-x}CoO_2$, Nat. Commun. **13**, 5810 (2022).

[10] Y. Zhu, J. C. Zheng, L. Wu, A. I. Frenkel, J. Hanson, P. Northrup, and W. Ku, Nanoscale disorder in $CaCu_3Ti_4O_{12}$: A new route to the enhanced dielectric response, Phys. Rev. Lett. **99**, 037602 (2007).

[11] J. Lee, M. Carbone, and W. Yin, Machine learning the spectral function of a hole in a quantum antiferromagnet, Phys. Rev. B **107**, 205132 (2023).

[12] K. Kaufmann, C. Zhu, A. S. Rosengarten, D. Maryanovsky, T. J. Harrington, E. Marin, and K. S. Vecchio, Crystal symmetry determination in electron diffraction using machine learning, Science **367**, 564 (2020).

[13] J. Munshi, A. Rakowski, B. H. Savitzky, S. E. Zeltmann, J. Ciston, M. Henderson, S. Cholia, A. M. Minor, M. K. Y. Chan, and C. Ophus, Disentangling multiple scattering with deep learning: Application to strain mapping from electron diffraction patterns, npj Comput. Mater. **8**, 254 (2022).

[14] J. Chen, H. Zhang, C. B. Wah, and W. Chen, Automated crystal system identification from electron diffraction patterns using multiview opinion fusion machine learning, Proc. Nat. Acad. Sci. USA **120**, e2309240120 (2023).

[15] R. Yuan, J. Zhang, L, He, and J.-M. Zuo, Training artificial neural networks for precision orientation and strain mapping using 4D electron diffraction datasets, Ultramicroscopy **231**, 113256 (2021).

[16] L. Tiong, J. Kim, S. S. Han, and D. Kim, Identification of crystal symmetry from noisy diffraction patterns by a shape analysis and deep learning, npj Comput. Mater. **6**, 196 (2020).

[17] C. Ophus, Four-dimensional scanning transmission electron microscopy (4D-STEM): From scanning nanodiffraction to ptychography and beyond, Microsc. Microanal. **25**, 563 (2019).

[18] J. Madsen, P. Liu, J. Kling, J. B. Wagner, T. W. Hansen, O. Winther, and J. Schiøtz, A deep learning approach to identify local structures in atomic-resolution transmission electron microscopy images, Adv. Theory Simul. **1**, 1800037 (2018).

[19] W. Xu and J. LeBeau, A deep convolutional neural network to analyze position averaged convergent beam electron diffraction patterns, Ultramicroscopy **188**, 59 (2018).

[20] J. Aguiar, M. L. Gong, R. R. Unocic, T. Tasdizen, and B. D. Miller, Decoding crystallography from high-resolution electron imaging and diffraction datasets with deep learning, Sci. Adv. **5**, eaaw1949 (2019).

[21] D. Torbunov, Y. Ren, L. Wu, and Y. Zhu, Parameter inference and uncertainty quantification with diffusion models: Extending CDI to 2D spatial conditioning, arXiv:2601.17224.

[22] P. Coppens, *X-Ray Charge Densities and Chemical Bonding* (Oxford University Press, New York, 1997).

[23] N. K. Hansen and P. Coppens, Testing aspherical atom refinements on small-molecule data sets, Acta Crystallogr. Sect. A **34**, 909 (1978).

[24] F. A. Parpia, C. F. Fischer, and I. P. Grant, GRASP92: A package for large-scale relativistic atomic structure calculations, Comput. Phys. Commun. **94**, 249 (1996).

[25] L. J. Wu, T. Vogt, H. Su, and J. W. Davenport, and J. Tafto, Valence-electron distribution in MgB_2 by accurate diffraction measurements and first-principles calculations, Phys. Rev. B **69**, 064501 (2004).

[26] T. Lippmann, P. Blaha, N. H. Andersen, H. F. Poulsen, T. Wolf, J. R. Schneider, and K.-H. Schwarz, Charge-density analysis of $YBa_2Cu_3O_{6.98}$. Comparison of theoretical and experimental results, Acta Crystallogr. Sect. A **59**, 437 (2003).

[27] E. A. Zhurova and V. G. Tsirelson, Electron density and energy density view on the atomic interactions in $SrTiO_3$, Acta Crystallogr. Sec. B-Struct. Sci. **58**, 567 (2002).

[28] K. He, X. Zhang, S. Ren and J. Sun, Deep residual learning for image recognition, in *2016 IEEE Conference on Computer Vision and Pattern Recognition (CVPR)* (IEEE, Las Vegas, NV, 2016), pp. 770–778.

[29] I. Loshchilov and F. Hutter, Decoupled weight decay regularization, in *7th International Conference on Learning Representations* (OpenReview.net, New Orleans, 2019).

[30] F. Zhu, D. Torbunov, Z. Jiang, T. Zhao, A. Yogarathnam, Y. Ren, and M. Yue, Diffusion model-based parameter estimation in dynamic power systems, Commun. Eng. (2026), doi: 10.1038/s44172-026-00670-z.

[31] J. Sohl-Dickstein, N. Maheswaranathan, and S. Ganguli, *ICML'15: Proceedings of the 32nd International Conference on Machine Learning* (ACM Digital, New York, 2015), Vol. 37, pp. 2256–2265.

[32] J. Ho, A. Jain, and P. Abbeel, Denoising diffusion probabilistic models, in *NIPS'20: Proceedings of the 34th International Conference on Neural Information Processing Systems* (ACM Digital, New York, 2020), pp. 6840–6851.

[33] T. Gneiting, F. Balabdaoui, and A. Raftery, Probabilistic forecasts, calibration and sharpness, J. R. Stat. Soc. B. Stat. Methodol. **69**, 243 (2007).

[34] V. Kuleshov, N. Fenner, and S. Ermon, Accurate uncertainties for deep learning using calibrated regression, in *Proceedings of the 35th International Conference on Machine Learning, Stockholm, Sweden*, Proceedings of Machine Learning Research, Vol. 80 (PMLR, 2018).

[35] Y. Huang, D. Torbunov, B. Viren, H. Yu, J. Huang, M. Lin, and Y. Ren, Unpaired image translation to mitigate domain shift in liquid argon time projection chamber detector responses, Mach. Learn.-Sci. Technol. **5**, 045021 (2024).

[36] H. Guan and M. Liu, Domain adaptation for medical image analysis: A survey, IEEE Trans. Biomed. Eng. **69**, 1173 (2022).

[37] J. Lehtinen, J. Munkberg, J. Hasselgren, S. Laine, T. Karras, M. Aittala, and T. Aila, *Proceedings of the 35th International Conference on Machine Learning, Stockholm, Sweden*, Proceedings of Machine Learning Research, Vol. 80 (PMLR, 2018).

[38] M. Guo, Y. Wu, C. M. Hobson, Y. Su, S. Qian, E. Krueger, R. Christensen, G. Kroeschell, J. Bui, M. Chaw, L. Zhang, *et al.*, Deep learning-based aberration compensation improves contrast and resolution in fluorescence microscopy, Nat. Commun. **16**, 313 (2025).

[39] I. Lobato, T. Friedrich, and S. Van Aert, Deep convolutional neural networks to restore single-shot electron microscopy images, npj Comput. Mater. **10**, 10 (2024).